Geophysical Research Letters

RESEARCH LETTER
10.1029/2024GL113117

Assessing the Duration of the Paleocene-Eocene Thermal Maximum

Victor A. Piedrahita[1,2,3], David Heslop[4], Andrew P. Roberts[4], Eelco J. Rohling[5,6], Simone Galeotti[7,8], Fabio Florindo[8,9], and Jinhua Li[1,2,3,10]

[1]Key Laboratory of Deep Petroleum Intelligent Exploration and Development, Institute of Geology and Geophysics, Chinese Academy of Sciences, Beijing, China, [2]Laboratory for Marine Geology, Qingdao Marine Science and Technology Center, Qingdao, China, [3]Southern Marine Science and Engineering Guangdong Laboratory, Zhuhai, China, [4]Research School of Earth Sciences, Australian National University, Canberra, ACT, Australia, [5]Department of Earth Sciences, Utrecht University, Utrecht, The Netherlands, [6]School of Ocean and Earth Science, National Oceanography Centre, University of Southampton, Southampton, UK, [7]Dipartimento di Scienze Pure e Applicate, Università Degli Studi di Urbino, Urbino, Italy, [8]Institute for Climate Change Solutions, Frontone, Pesaro e Urbino, Italy, [9]Istituto Nazionale di Geofisica e Vulcanologia, Rome, Italy, [10]College of Earth and Planetary Sciences, University of Chinese Academy Sciences, Beijing, China

Key Points:

- We produce a statistically defined detection limit for the carbon isotope excursion (CIE) of the Paleocene-Eocene Thermal Maximum (PETM)
- Our protocol establishes the time range over which the PETM CIE is detected in stable carbon isotope ($\delta^{13}C$) records
- Statistical analyses reveal a longer ($268.8^{+21.2}/_{-20.5}$ kyr) PETM CIE duration than previous estimates (~120–230 kyr)

Supporting Information:

Supporting Information may be found in the online version of this article.

Correspondence to:

J. Li,
lijinhua@mail.iggcas.ac.cn

Citation:

Piedrahita, V. A., Heslop, D., Roberts, A. P., Rohling, E. J., Galeotti, S., Florindo, F., & Li, J. (2025). Assessing the duration of the Paleocene-Eocene Thermal Maximum. *Geophysical Research Letters*, *52*, e2024GL113117. https://doi.org/10.1029/2024GL113117

Received 21 OCT 2024
Accepted 12 MAR 2025

Author Contributions:

Conceptualization: Victor A. Piedrahita, Andrew P. Roberts, Eelco J. Rohling, Simone Galeotti
Formal analysis: Victor A. Piedrahita
Funding acquisition: Victor A. Piedrahita, David Heslop, Andrew P. Roberts, Jinhua Li
Investigation: Victor A. Piedrahita
Methodology: Victor A. Piedrahita, David Heslop, Andrew P. Roberts, Eelco J. Rohling
Resources: Simone Galeotti, Fabio Florindo, Jinhua Li
Software: David Heslop
Validation: Victor A. Piedrahita, David Heslop

Abstract The Paleocene-Eocene Thermal Maximum (PETM) was a climate/carbon cycle perturbation recognized in stable carbon isotope ($\delta^{13}C$) records with a negative carbon isotope excursion (CIE). The PETM CIE termination has been associated with a $\delta^{13}C$ inflection with pre-PETM-like values referred to as the *G* point. However, the *G* point approach has produced variable PETM CIE duration estimates (~120–230 kyr), which reflects a need to test its reliability. Here, we apply statistical analyses to existing $\delta^{13}C$ records and reveal that the *G* point is sensitive to underlying $\delta^{13}C$ uncertainties. We generate a probabilistic-based CIE detection limit, which constrains the time range over which the PETM is detected in $\delta^{13}C$ records. This protocol reveals a protracted CIE recovery (>145 kyr) that accounts for a $268.8^{+21.2}/_{-20.5}$ kyr PETM CIE duration. Our new duration estimate exceeds previous values, which confirms the potential of extreme carbon cycle perturbations to cause long-lasting carbon cycle disruptions.

Plain Language Summary Ancient global warming events can be used to better understand future impacts of anthropogenic global warming; however, the extent to which a massive carbon cycle perturbation can disrupt the carbon cycle remains elusive. Here, we constrain the duration of the largest climate/carbon cycle perturbation of the last ~65 Ma, the Paleocene-Eocene Thermal Maximum (PETM). The PETM duration has been widely studied using its signature in stable carbon isotope ($\delta^{13}C$) records, a negative carbon isotope excursion (CIE). We find that the previous concept to estimate the PETM CIE duration using $\delta^{13}C$ signals is not replicable. Therefore, we develop a statistical approach that accounts for the recognizable PETM CIE signal. This new concept reveals a $268.8^{+21.2}/_{-20.5}$ kyr PETM CIE duration, which is longer than previous ~120–230 kyr estimates and suggests that carbon cycle perturbations have protracted impacts on the natural carbon cycle.

1. Introduction

Anthropogenic global warming is driven by exceptional carbon emission rates that have not been recorded in natural records over the past ~65 Ma (Allen et al., 2009; Matthews et al., 2009; Solomon et al., 2009; Zeebe et al., 2016). This human-driven climate perturbation is expected to disrupt the natural carbon cycle for a ~3–165 kyr period, which is defined as the anthropogenic carbon lifetime (Archer, 2005; Archer et al., 2009; Eby et al., 2009; Lord et al., 2016; Montenegro et al., 2007; Zeebe, 2013). This wide range of estimates is given by *e*-folding timescales of exponential decay functions that describe carbon removal trajectories based on carbon cycle models (Archer et al., 2009). However, the temporal extent to which a carbon release disturbs the carbon cycle remains uncertain because carbon cycle models depend on variable setup conditions such as carbon injection magnitudes, inclusion of time-dependent positive carbon cycle feedbacks, and/or addition of contrasting carbon removal mechanisms (Archer, 2005; Archer et al., 2009; Colbourn et al., 2015; Eby et al., 2009; Lord et al., 2016; Zeebe, 2013; Zeebe & Zachos, 2013). Geological global warming events offer opportunities to gauge natural recovery timescales from major carbon cycle perturbations (e.g., Bowen & Zachos, 2010; Penman & Zachos, 2018; Piedrahita et al., 2023; Zeebe et al., 2017). Here, we make such an assessment for the greatest Cenozoic carbon cycle perturbation, the Paleocene-Eocene Thermal Maximum (PETM; ~56 Ma).

10.1029/2024GL113117

Visualization: Victor A. Piedrahita, David Heslop, Simone Galeotti, Fabio Florindo, Jinhua Li
Writing – original draft: Victor A. Piedrahita
Writing – review & editing: David Heslop, Andrew P. Roberts, Eelco J. Rohling, Simone Galeotti, Fabio Florindo, Jinhua Li

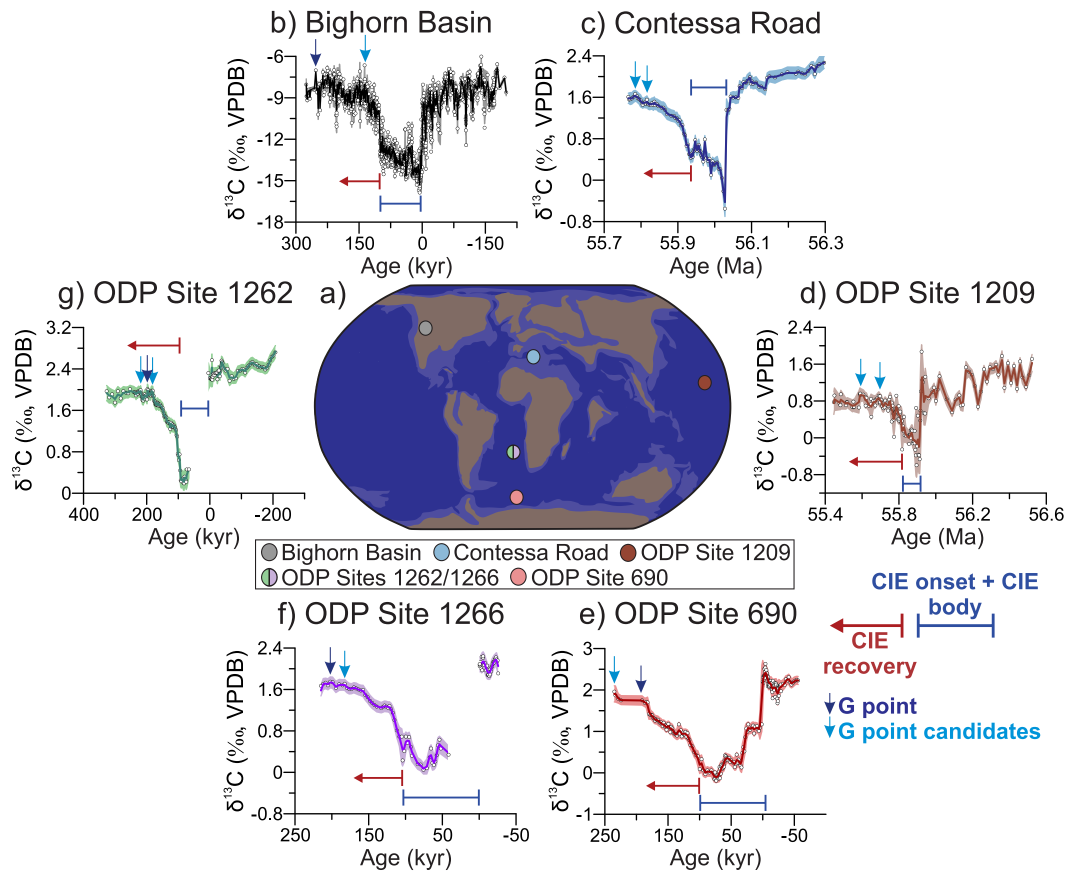

Figure 1. (a) Paleogeographic reconstruction at ~56 Ma (Pogge von Strandmann et al., 2021) with locations of the studied Paleocene-Eocene Thermal Maximum (PETM) $\delta^{13}C$ records from (b) Bighorn Basin, (c) Contessa Road, (d) ODP Site 1209, (e) ODP Site 690, (f) ODP Site 1266, and (g) ODP Site 1262. White dots represent raw data; continuous dark lines indicate the mean $\delta^{13}C$, with envelopes surrounding these lines indicating ±2 standard error (2SE) intervals. Horizontal lines for each record represent different PETM carbon isotope excursion (CIE) phases. Dark- and sky-blue arrows indicate the G point according to previous studies (van der Meulen et al., 2020; Westerhold, Röhl, Wilkens, et al., 2018) and similar $\delta^{13}C$ inflections referred to as G point candidates, respectively.

The Paleocene-Eocene Thermal Maximum (PETM) was a global warming event that caused a ~5–9°C temperature increase, ocean acidification, and major ecological disruption (McInerney & Wing, 2011; Secord et al., 2012; Wing et al., 2005; Zachos et al., 2005). This event was triggered by a ~3,000–20,000 Pg injection of isotopically light carbon from a reservoir external to the climate system (Elling et al., 2019; Gutjahr et al., 2017; Haynes & Hönisch, 2020; McInerney & Wing, 2011), which punctuated a long-term hothouse state with similar temperatures to those projected by the shared socio-economic pathway (SSP) 8.5 of the Intergovernmental Panel on Climate Change (IPCC) over the next three centuries (IPCC, 2021; Westerhold et al., 2020). The lower end of PETM carbon mass estimates is close to the 2,390 ± 240 Pg of anthropogenic CO_2 released from 1850 to 2019 (IPCC, 2021), and the potential ~5,000 Pg of carbon predicted to result from fossil fuel consumption over upcoming centuries (Rogner, 1997). However, carbon cycle models and cyclostratigraphic frameworks suggest that PETM carbon emissions were an order of magnitude slower than current anthropogenic emissions (Kirtland Turner et al., 2017; Li et al., 2022; Zeebe et al., 2016). These observations indicate that human-induced carbon emissions, which occur along with an increasing temperature trend, are likely to cause a similarly dramatic carbon cycle perturbation through activation of negative carbon cycle feedbacks (Gingerich, 2019). Hence, the PETM may be used to better understand possible anthropogenic influences on the natural carbon cycle (McInerney & Wing, 2011).

The PETM is recognized in geological stable carbon isotope ($\delta^{13}C$) records by a negative carbon isotope excursion (CIE) that is divided into different phases (Figure 1; McInerney & Wing, 2011). An initial PETM CIE onset phase is represented by a sudden $\delta^{13}C$ drop that indicates a massive light carbon injection with a ~4–21 kyr duration (see Supporting Information S1; Murphy et al., 2010; Zeebe et al., 2016; Kirtland Turner et al., 2017; Li et al., 2022). This phase was followed by a so-called PETM CIE body phase, which was a ~100 kyr-long period of ongoing greenhouse gas emissions that resulted from volcanic activity, oxidation of remobilized sedimentary fossil carbon, decline of terrestrial biosphere stocks, and/or thermal destabilization of methane hydrates, thermogenic methane or permafrost (see Supporting Information S1; Bowen, 2013; Bowen & Zachos, 2010; DeConto et al., 2012; Frieling et al., 2016; Kender et al., 2021; Lyons et al., 2019; Zeebe et al., 2009). These light carbon injections during the PETM CIE body caused contrasting regional $\delta^{13}C$ responses with prolonged intervals of low $\delta^{13}C$ values in some records, and multiple $\delta^{13}C$ increases and decreases in others (Figures 1b–1g).

The PETM CIE body was followed by the PETM recovery, which was a carbon sequestration period indicated by a transition from lower to higher $\delta^{13}C$ values (Figures 1b–1g; see Supporting Information S1). This ubiquitous pattern has been used to represent PETM carbon removal trajectories with exponential decay fits (Bowen, 2013; Bowen & Zachos, 2010; Piedrahita et al., 2023), which have *e*-folding timescales of ~8–38 kyr that are an order of magnitude shorter than those for silicate weathering (Bowen, 2013; Colbourn et al., 2015; Lord et al., 2016; Piedrahita et al., 2023). Such recovery *e*-folding timescales have been associated with accelerated light carbon removal promoted by optimized terrestrial biosphere carbon uptake and the oceanic biological pump (Bowen, 2013; Bowen & Zachos, 2010; Komar & Zeebe, 2017; Ma et al., 2014).

Proxy data reveal that accelerated organic carbon burial occurred in the initial ~30–40 kyr of the PETM recovery phase (Bowen & Zachos, 2010; Ma et al., 2014). This interval gave way—in accordance with exponential decay functions (Bowen & Zachos, 2010; Piedrahita et al., 2023)—to a longer-term PETM CIE recovery trajectory that eventually ended the CIE. Duration estimates for the PETM CIE recovery range from ~40 to ~120 kyr, assuming that it ended at the so-called *G* point (Giusberti et al., 2007; Murphy et al., 2010; Röhl et al., 2000, 2007; van der Meulen et al., 2020; Westerhold, Röhl, Wilkens, et al., 2018). The *G* point is typically identified arbitrarily as the inflection point where $\delta^{13}C$ became similar to pre-PETM $\delta^{13}C$ values, and has been used to obtain PETM CIE duration estimates in the 120–230 kyr range (see Supporting Information; Aziz et al., 2008; Farley & Eltgroth, 2003; Giusberti et al., 2007; Murphy et al., 2010; Röhl et al., 2000, 2007; van der Meulen et al., 2020; Westerhold, Röhl, Wilkens, et al., 2018; Zeebe & Lourens, 2019).

The wide range of PETM CIE duration estimates may partially result from a lack of consistent criteria to select the *G* point within noisy $\delta^{13}C$ records (Figures 1b–1g). Here, we study the PETM CIE recovery interval in well-resolved sedimentary sections to better identify the bounds of the $\delta^{13}C$ anomaly that defines the PETM CIE. We present probabilistic assessments using available high-resolution $\delta^{13}C$ records and age models for Bighorn Basin (North America), Contessa Road (western Tethys Ocean), and Ocean Drilling Program (ODP) Sites 1209 (northwestern Pacific Ocean), 690 (Southern Ocean), 1262, and 1266 (South Atlantic Ocean) to assess the reliability of the *G* point approach and to provide a statistical protocol to estimate the PETM CIE duration.

2. Materials and Methods

2.1. Study Sites

We study here one terrestrial and five marine PETM sedimentary sections with high-resolution $\delta^{13}C$ records, which allow a global assessment of the PETM CIE duration and clear identification of the event phases. These PETM sections also have well-developed age models, whose reliability has been demonstrated in previous studies (see Supporting Information S1). Therefore, we do not generate new age models or $\delta^{13}C$ records and use these available data sets to perform probabilistic assessments (*see below*). The studied terrestrial site corresponds to a Bighorn Basin composite section with a high-resolution $\delta^{13}C$ carbonate nodule record (Figure 1b; van der Meulen et al., 2020). We also study bulk-rock $\delta^{13}C$ records from marine sediment sections such as the Contessa Road (western Tethys), ODP Site 690 (Southern Ocean), and ODP Sites 1262 and 1266 (South Atlantic Ocean), and a benthic foraminiferal (*Nuttallides truempyi*) $\delta^{13}C$ record from ODP Site 1209 (northwestern Pacific Ocean) (see Supporting Information S1; Giusberti et al., 2009; Galeotti et al., 2010; Littler et al., 2014; Piedrahita et al., 2022, 2023; Röhl et al., 2007; Thomas, 1990; Westerhold et al., 2007, 2011; Westerhold, Röhl, Wilkens, et al., 2018; Westerhold, Röhl, Donner, et al., 2018; Zachos et al., 2005).

2.2. Probabilistic Uncertainty Assessments

2.2.1. $\delta^{13}C$ Error Propagation

PETM $\delta^{13}C$ records have been typically studied using raw data, without considering analytical and chronological uncertainties. Here, we apply a Monte Carlo-based protocol for error propagation in $\delta^{13}C$ records from Bighorn Basin and ODP Sites 1209, 690, 1262, and 1266. A similar probabilistic assessment for the Contessa Road $\delta^{13}C$ record (Piedrahita et al., 2023) is also included here. Given the lack of reported analytical uncertainties, Bighorn Basin and ODP Sites 1209, 690, 1262, and 1266 $\delta^{13}C$ datapoints were assigned 0.06‰ standard deviations (1σ), which represents the external reproducibility of most $\delta^{13}C$ analyses (e.g., Piedrahita et al., 2023). Next, age errors were included based on each age model as follows. Half the age spacing between successive samples was considered as a standard deviation (1σ) for ODP Site 1262 because of its relatively uniform measurement resolution across its $\delta^{13}C$ record. The other PETM $\delta^{13}C$ records have contrasting measurement resolutions between their CIE phases–i.e., half the age spacing between successive samples range from ∼0.4 kyr to ∼13 kyr–which hinders application of our Monte Carlo-based approach. Therefore, we assigned the average half age spacing between successive samples as the 1σ standard deviation for Bighorn Basin (1σ = 0.3 kyr), ODP Site 1209 (1σ = 3.7 kyr), ODP Site 690 (1σ = 1.5 kyr), and ODP Site 1266 (1σ = 2.1 kyr). We then performed a Monte Carlo-based re-sampling that generates 10,000 random data points within the $\delta^{13}C$ and age uncertainties. This protocol produces empirical $\delta^{13}C$ distributions at each age step, from which the mean and standard error were estimated. Data were reviewed systematically after Monte Carlo simulations to avoid age reversals and to maintain stratigraphic order. Finally, data were interpolated to the fixed age points of each age model, which allowed generation of probabilistic-based $\delta^{13}C$ records.

2.2.2. Exponential Decay Functions Across the PETM CIE Recovery Interval

Exponential decay functions were fitted to the probabilistic-based $\delta^{13}C$ records to assess $\delta^{13}C$ trajectories during the PETM CIE recovery (e.g., Bowen, 2013; Bowen & Zachos, 2010; Piedrahita et al., 2023). Specifically, 10,000 least-squares exponential decay fits, expressed as $f(x,\beta) = \beta_0 \cdot e^{\beta_1 \cdot x} + \beta_2$, were generated using Monte Carlo simulations. Probability distributions of the fitted functions were obtained at each time-step and the 50th percentile (median) and 2.5th to 97.5th percentiles (95% confidence interval) were estimated. *e*-folding timescales were estimated from the equation coefficients (*e*-folding $= 1/|\beta_1|$), and reduced chi-square (χ^2) statistics were used to assess the goodness of the modeled exponential decay functions with respect to the analyzed data.

2.2.3. Bootstrap Resampling

To obtain a single numerical estimate for the PETM CIE duration and its recovery, different groups of age estimates obtained here (*see Discussion*) were used to generate 10,000 iterations via bootstrapping with replacement. The median and 95% confidence interval were estimated from the empirical distributions produced for each data group.

3. Results

Our probabilistic $\delta^{13}C$ records highlight key features of the original PETM $\delta^{13}C$ records. At Bighorn Basin, Contessa Road, and ODP Site 1209, a sudden $\delta^{13}C$ drop marks the CIE onset (Figures 1b–1d). A similar $\delta^{13}C$ decrease is identified at ODP Site 690; however, $\delta^{13}C$ decreased continuously until stabilizing ∼70 kyr after the onset (Figure 1e). ODP Sites 1262 and 1266 do not have $\delta^{13}C$ data at the CIE onset (Figures 1f and 1g) due to extensive $CaCO_3$ dissolution caused by ocean acidification during the initial light carbon injection (Zachos et al., 2005). The PETM CIE onset is followed by the body phase, which at Bighorn Basin and ODP Sites 690, 1262, and 1266 is represented by sustained low $\delta^{13}C$ values (Figures 1b, 1e–1g). The CIE body at Contessa Road has a gradual $\delta^{13}C$ increase following the CIE onset and is punctuated by a second smaller $\delta^{13}C$ drop ∼80 kyr after the PETM CIE onset (Piedrahita et al., 2023). A similar pattern is identified in the probabilistic $\delta^{13}C$ record from ODP Site 1209 although this section does not contain a second $\delta^{13}C$ drop (Figures 1c and 1d). The CIE recovery in all sections is marked by a continuous, irreversible, $\delta^{13}C$ increase that starts ∼100 kyr after the CIE onset (Figures 1b–1g).

Exponential decay functions fitted to CIE recovery intervals of the $\delta^{13}C$ records (Figure 2) reveal similar *e*-folding timescales for Contessa Road, and ODP Sites 1209, 1262, and 1266 ($34.6^{+3.3}/_{-4.0}$ kyr to $43.1^{+2.6}/_{-2.5}$ kyr

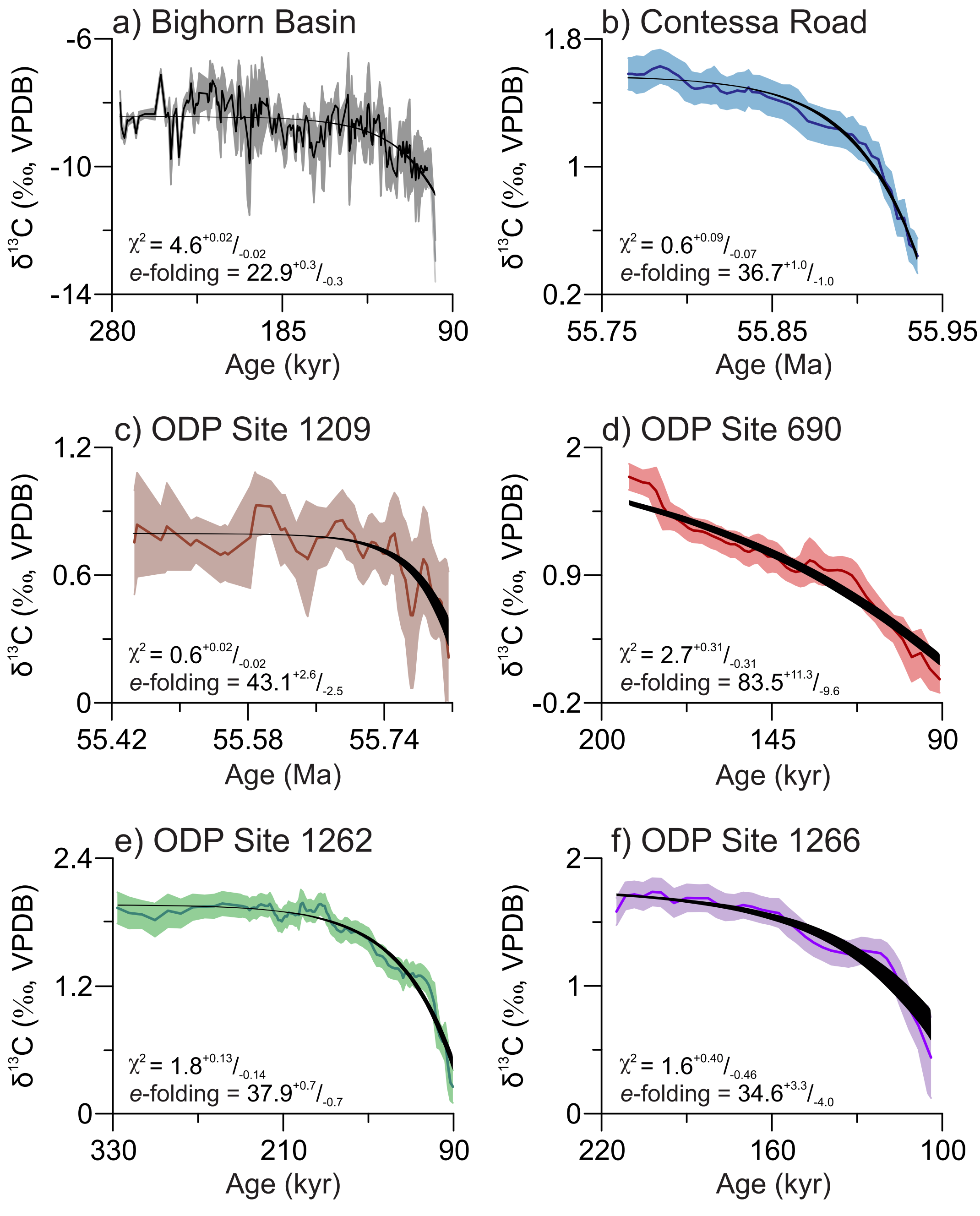

Figure 2. Exponential decay functions presented in terms of their 95% confidence intervals (black) for the PETM CIE recovery interval at (a) Bighorn Basin, (b) Contessa Road, (c) ODP Site 1209, (d) ODP Site 690, (e) ODP Site 1262, and (f) ODP Site 1266. Background $\delta^{13}C$ records are indicated in dark (mean) and light shading (±2 standard error (2SE)). Age scales are based on the PETM CIE recovery onset according to the age model for each studied section.

(median ± 95% confidence interval). χ^2 values for exponential fits to the Contessa Road, and ODP Sites 1209, 1262, and 1266 data range from $0.6^{+0.02}/_{-0.02}$ to $1.8^{+0.13}/_{-0.14}$, which suggests that the modeled exponential decay functions properly fit the analyzed data (Figures 2b and 2c, 2d–2e, 3a–3b). At Bighorn Basin, the *e*-folding is slightly smaller ($22.9^{+0.3}/_{-0.3}$ kyr), while it is higher at ODP Site 690 (*e*-folding = $83.5^{+11.3}/_{-9.6}$ kyr) (Figures 2d and 3a). The latter two sections have χ^2 values > 2.7, which are higher than those from the remaining records, and suggest that exponential decay functions do not accurately fit the analyzed data (Figures 2a and 2d, 3a, 3b).

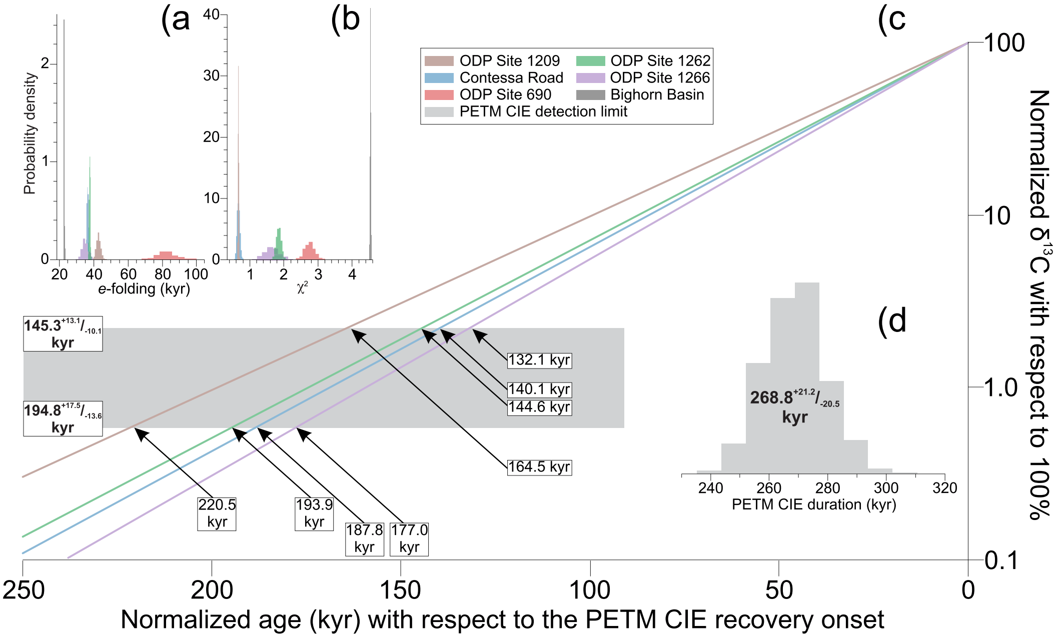

Figure 3. Probability density distributions for (a) *e*-folding and (b) χ^2 values of exponential decay functions from each studied $\delta^{13}C$ record. (c) Modeled exponential decay functions for normalized $\delta^{13}C$ values (100%) that decay at rates defined by *e*-folding timescales (ODP Site 1209 = 43.1 kyr, ODP Site 1262 = 37.9 kyr, Contessa Road = 36.7 kyr and ODP Site 1266 = 34.6 kyr). The PETM CIE detection limit is indicated by a gray rectangle that is limited by the 0.6%–2.2% interval (see Supporting Information S1). Durations in white rectangles represent PETM CIE recovery duration estimates for each section, while values in bold letters represent probabilistic-based PETM CIE recovery duration estimates for each PETM CIE detection boundary. (d) Probability density distribution for the PETM CIE duration. The median and 95% confidence interval of this distribution are indicated as our probabilistic-based PETM CIE duration estimate.

4. Discussion

4.1. $\delta^{13}C$ Recovery Patterns and *G* Point Reliability

The exponential decay approach used here for the PETM CIE recovery produces adequate fits ($\chi^2 < \sim1.8$) with overlapping *e*-folding timescales (∼35–43 kyr; Figures 3a and 3b) for Contessa Road and ODP Sites 1209, 1262, and 1266 despite the different CIE body features (Figures 1c and 1d, 1f and 1g), paleogeographic positions, paleowater depths, and microfossil assemblages of these sections (see Supporting Information S1). These exponential $\delta^{13}C$ recovery patterns are similar to those identified in previous carbon removal trajectory assessments following PETM light carbon injections, which reflects a generalized $\delta^{13}C$ pattern during the PETM CIE recovery phase (Bowen, 2013; Bowen & Zachos, 2010; Komar & Zeebe, 2017; Penman et al., 2020; Piedrahita et al., 2023). However, PETM CIE recovery at Bighorn Basin and ODP Site 690 cannot be represented by exponential decay functions ($\chi^2 > \sim2.7$; Figure 3b), which contrasts with prior assessments for the same sites (e.g., Bowen & Zachos, 2010). These differences may result from addition of further $\delta^{13}C$ datapoints that have modified previously evaluated data sets. This may be the case for the Bighorn Basin section, which has a noisy $\delta^{13}C$ record that may hinder exponential fitting across the PETM CIE recovery (Figure 2a). Alternatively, inclusion of our error propagation protocol in the ODP 690 analysis could limit the use of exponential decay fits due to a measurement gap in the recovery phase of this site. Contrasting Bighorn Basin and ODP Site 690 CIE recovery patterns with respect to the other sites may also indicate regional controls on these $\delta^{13}C$ records−that is, local hydroclimate changes that impact chemical weathering and/or organic carbon removal−, and/or variable marine and terrestrial $\delta^{13}C$ responses to global carbon removal trends. Given these limitations, we exclude exponential decay fits for Bighorn Basin and ODP Site 690 from further analysis here.

Similarities between PETM CIE recovery patterns at Contessa Road and ODP Sites 1209, 1262, and 1266 suggest that relative PETM CIE durations, and, therefore, the *G* point, should be almost identical among $\delta^{13}C$ records. However, $\delta^{13}C$ inflections similar to the *G* point occur at multiple ages (Figures 1c and 1d, 1f and 1g). Well-developed exponential decay fits across these sites reveal gradual $\delta^{13}C$ flattening across the PETM CIE recovery instead of a clear *G* point $\delta^{13}C$ inflection (Figures 1b–1g and 2). Furthermore, our probabilistic assessments indicate that the interval where the *G* point has been recognized (e.g., Murphy et al., 2010; Röhl et al., 2007; van der Meulen et al., 2020; Westerhold, Röhl, Wilkens, et al., 2018; Zeebe & Lourens, 2019) consists of a series of datapoints with overlapping uncertainties (see error envelopes in Figures 1b–1g). This reveals that the *G* point detection approach is sensitive to noise and underlying $\delta^{13}C$ signal uncertainties, which limits the value of this protocol to determine the PETM CIE endpoint. $\delta^{13}C$ error envelopes also indicate overlapping values across the PETM CIE body, which hinders identification of $\delta^{13}C$ inflections related to PETM tie points that were recognized in prior PETM CIE age models (see Supporting Information S1; Bains et al., 1999). Probabilistic assessments still allow clear recognition of the PETM CIE onset, body and recovery (Figures 1b–1g), and they also reveal that subjective, visual identification of a particular $\delta^{13}C$ inflection with pre-PETM-like values during the PETM CIE recovery cannot be used to recognize PETM CIE termination.

4.2. A New Statistical Approach to Estimate PETM CIE Duration

Exponential $\delta^{13}C$ recovery functions reveal a protracted PETM CIE duration. Our ∼30–40 kyr *e*-folding timescales of exponential $\delta^{13}C$ recovery fits are similar to those of previous studies, and consequently reflect accelerated carbon removal compared to silicate weathering (>100 kyr *e*-folding values; Bowen & Zachos, 2010; Bowen, 2013; Colbourn et al., 2015; Lord et al., 2016; Penman et al., 2020; Piedrahita et al., 2023). We interpret our estimates to depend on enhanced organic carbon burial, which was enhanced during a ∼30–40 kyr period at the commencement of the PETM CIE recovery phase (Bowen & Zachos, 2010; Ma et al., 2014). However, organic carbon sequestration occurred alongside with optimized chemical weathering, which resulted from exceptional PETM warming (Penman et al., 2016, 2020; Pogge von Strandmann et al., 2021; Torfstein et al., 2010); hence, we infer that accelerated organic carbon uptake and long-term chemical weathering slowly diminished the PETM CIE in $\delta^{13}C$ records, and stabilized the carbon cycle (Penman et al., 2016, 2020; Pogge von Strandmann et al., 2021).

The interval of gradual $\delta^{13}C$ flattening following accelerated organic carbon uptake is used here to generate a PETM CIE detection limit based on statistical and geological criteria. This method allows estimation of the extent to which the PETM CIE is recognized in $\delta^{13}C$ records. Initially, we transferred the 95% confidence interval of each datapoint from accurate exponential decay functions to a percentage with respect to the median (see Supporting Information S1). The average 95% confidence interval was estimated for each site, excluding initial periods equivalent to *e*-folding timescales, where $\delta^{13}C$ signals rapidly increase and are not gradually flattened. Average errors of 0.6% for Contessa Road and ODP Site 1262, 1.0% for ODP Site 1209%, and 2.2% for ODP Site 1266 were obtained. The highest and lowest average errors were assumed to represent the lower and upper boundaries of an error threshold below which an initial magnitude of 100% does not represent statistical exceedances (see Supporting Information S1). Following this protocol, a detection limit that accounts for the recognizable PETM CIE recovery signal in $\delta^{13}C$ records can be defined by an upper (2.2%) and a lower (0.6%) boundary that represent ∼4 and ∼5 *e*-folding timescales, respectively (Figure 3c). To obtain PETM CIE recovery duration estimates, the $\delta^{13}C$ datapoint that marks the PETM CIE recovery onset was normalized to 100% and assigned a 0 kyr age. This magnitude was forced to decay at different rates defined by the *e*-folding timescales of Contessa Road and ODP Sites 1209, 1262, and 1266. This approach reveals PETM CIE recovery duration estimates of ∼132.1 kyr, ∼140.1 kyr, ∼144.6 and ∼164.5 kyr for the upper recognizable CIE recovery boundary, and ∼177.0 kyr, ∼187.8 kyr, ∼193.9 kyr and ∼220.5 for the lower PETM CIE detection limit (Figure 3c). Via bootstrap resampling (*see Materials and methods*), single PETM CIE recovery duration estimates for the upper ($145.3^{+13.1}/_{-10.1}$ kyr) and lower ($194.8^{+17.5}/_{-13.6}$ kyr) CIE detection boundaries were obtained (Figure 3c).

4.3. A Longer PETM CIE Duration

Our new PETM CIE recovery duration estimates are longer than those of previous studies (∼40–120 kyr) (Aziz et al., 2008; Farley & Eltgroth, 2003; Giusberti et al., 2007; Murphy et al., 2010; van der Meulen et al., 2020; Westerhold et al., 2007; Zeebe & Lourens, 2019). Considering that most carbon cycle models reveal carbon removal periods exceeding those of carbon injections (e.g., Archer, 2005; Eby et al., 2009; Montenegro et al., 2007; Zeebe, 2013), and given the large magnitude of PETM carbon releases and their associated ∼100 kyr-long CIE body (Elling et al., 2019; McInerney & Wing, 2011), our PETM CIE recovery duration estimates seem plausible and can be seen within the context of organic carbon removal and chemical weathering (e.g., Penman et al., 2020). These longer PETM CIE recovery duration estimates can be used to constrain locally the PETM CIE duration for Contessa Road (∼236.7–284.5 kyr), and ODP Sites 1209 (∼268.5–324.5 kyr), 1262 (∼235.1–284.4 kyr), and 1266 (∼236.0–281.0 kyr). Using bootstrap resampling (*see Materials and methods*), a $268.8^{+21.2}/_{-20.5}$ kyr (median ± 95% confidence interval; Figure 3d) PETM CIE duration estimate is produced. This value may be modified by addition of further well-resolved $\delta^{13}C$ records; however, the global coverage of our assessment, and the inclusion of a probabilistic-based approach that indicates similar PETM $\delta^{13}C$ recovery rates among several locations, suggest that our new estimate is reliable. Our estimated $268.8^{+21.2}/_{-20.5}$ kyr PETM CIE duration overlaps within uncertainties some previous values of $217^{+44}/_{-31}$ kyr and 231 ± 22 kyr (Giusberti et al., 2007; Murphy et al., 2010), but is substantially longer than the ∼120–220 kyr durations obtained from most studies (Aziz et al., 2008; Farley & Eltgroth, 2003; Röhl et al., 2000, 2007; van der Meulen et al., 2020; Westerhold, Röhl, Wilkens, et al., 2018; Zeebe & Lourens, 2019).

Our new probabilistic PETM CIE duration estimate corroborates the view that a massive carbon cycle perturbation is likely to disrupt the natural carbon cycle for hundreds of thousands of years. However, our ∼35–43 kyr *e*-folding timescales have been reproduced successfully only by carbon cycle models with *e*-folding values that exceed common <10 kyr anthropogenic carbon lifetime estimates (Archer, 2005; Archer et al., 2009; Eby et al., 2009; Lord et al., 2016; Montenegro et al., 2007; Zeebe, 2013). Hence, the long duration of the recognizable PETM CIE signal in $\delta^{13}C$ records reveals that a massive carbon cycle perturbation, which can be triggered in association with a future SSP 8.5 global warming scenario (Gingerich, 2019; IPCC, 2021; Zeebe, 2013), is likely to disrupt the carbon cycle over periods that are longer than those predicted by most carbon cycle models. Although detailed comparison between anthropogenic carbon and PETM $\delta^{13}C$ *e*-folding timescales is complicated (e.g., Archer, 2005; Eby et al., 2009; Montenegro et al., 2007; Zeebe, 2013), our duration estimates for the PETM CIE recovery far exceed societally relevant timescales, which emphasizes the pressing need to limit and reverse anthropogenic greenhouse gas emissions.

5. Conclusions

PETM CIE recovery intervals at Contessa Road, and ODP sites 1209, 1262, and 1266 can be represented by exponential decay functions with similar *e*-folding timescales that coincide with widespread acceleration of organic carbon burial. Long-term carbon sequestration following this period should have removed the recognizable PETM CIE signal in $\delta^{13}C$ records; however, the PETM CIE endpoint cannot be determined unambiguously using the traditional *G* point concept because of its sensitivity to noise and uncertainty. We describe a new protocol associated with a CIE detection limit that produces PETM CIE recovery duration estimates of $145.3^{+13.1}/_{-10.1}$ kyr and $194.8^{+17.5}/_{-13.6}$ kyr, which result in a $268.8^{+21.2}/_{-20.5}$ kyr PETM CIE duration. This new estimate compared to previous studies reveals that extreme carbon cycle perturbations are likely to disrupt the carbon cycle for longer periods that those projected by most carbon cycle models.

Conflict of Interest

The authors declare no conflicts of interest relevant to this study.

Data Availability Statement

The original $\delta^{13}C$ data and age models of Bighorn Basin, Contessa Road, and ODP Sites 690, 1209, 1262 and 1266 can be found in Bains et al. (1999), Zachos et al. (2005), Röhl et al. (2007), Westerhold et al. (2007, 2011), Westerhold, Röhl, Wilkens, et al. (2018), Westerhold, Röhl, Donner, et al. (2018), van der Meulen et al. (2020), and Piedrahita et al. (2023). These data were compiled for this study and presented in Piedrahita et al. (2025), alongside with the code used to develop the exponential decay functions.

Acknowledgments
This study was supported financially by the National Natural Science Foundation of China (Grants 42225402 and W2433104), the Innovation Group Project of Southern Marine Science and Engineering Guangdong Laboratory (Zhuhai) (Grant 311022004), the Australian Research Council (Grant DP190100874), the China Postdoctoral Science Foundation (Grant 2024M753205), and the Chinese Academy of Sciences through an International Postdoctoral Exchange Fellowship (Talent introduction program) and an IGGCAS International Fellowship for Postdoctoral Researchers. We thank three anonymous reviewers and the editor, Dr Sarah Feakins, for their suggestions that improved this manuscript.

References

Allen, M. R., Frame, D. J., Huntingford, C., Jones, C. D., Lowe, J. A., Meinshausen, M., & Meinshausen, N. (2009). Warming caused by cumulative carbon emissions towards the trillionth tonne. *Nature*, *458*(7242), 1163–1166. https://doi.org/10.1038/nature08019

Archer, D. (2005). Fate of fossil fuel CO_2 in geologic time. *Journal of Geophysical Research*, *110*(C9), C09S05. https://doi.org/10.1029/2004JC002625

Archer, D., Eby, M., Brovkin, V., Ridgwell, A., Cao, L., Mikolajewicz, U., et al. (2009). Atmospheric lifetime of fossil fuel carbon dioxide. *Annual Review of Earth and Planetary Sciences*, *37*(1), 117–134. https://doi.org/10.1146/annurev.earth.031208.100206

Aziz, H. A., Hilgen, F. J., van Luijk, G. M., Sluijs, A., Kraus, M. J., Pares, J. M., & Gingerich, P. D. (2008). Astronomical climate control on paleosol stacking patterns in the upper paleocene-lower eocene willwood formation, Bighorn Basin, Wyoming. *Geology*, *36*(7), 531–534. https://doi.org/10.1130/G24734A.1

Bains, S., Corfield, R. M., & Norris, R. D. (1999). Mechanisms of climate warming at the end of the Paleocene. *Science*, *285*(5428), 724–727. https://doi.org/10.1126/science.285.5428.724
Bowen, G. J. (2013). Up in smoke: A role for organic carbon feedbacks in paleogene hyperthermals. *Global and Planetary Change*, *109*, 18–29. https://doi.org/10.1016/j.gloplacha.2013.07.001
Bowen, G. J., & Zachos, J. C. (2010). Rapid carbon sequestration at the termination of the palaeocene-eocene thermal maximum. *Nature Geoscience*, *3*(12), 866–869. https://doi.org/10.1038/ngeo1014
Colbourn, G., Ridgwell, A., & Lenton, T. M. (2015). The time scale of the silicate weathering negative feedback on atmospheric CO_2. *Global Biogeochemical Cycles*, *29*(5), 583–596. https://doi.org/10.1002/2014GB005054
DeConto, R. M., Galeotti, S., Pagani, M., Tracy, D., Schaefer, K., Zhang, T., et al. (2012). Past extreme warming events linked to massive carbon release from thawing permafrost. *Nature*, *484*(7392), 87–91. https://doi.org/10.1038/nature10929
Eby, M., Zickfeld, K., Montenegro, A., Archer, D., Meissner, K. J., & Weaver, A. J. (2009). Lifetime of anthropogenic climate change: Millennial time scales of potential CO_2 and surface temperature perturbations. *Journal of Climate*, *22*(10), 2501–2511. https://doi.org/10.1175/2008JCLI2554.1
Elling, F. J., Gottschalk, J., Doeana, K. D., Kusch, S., Hurley, S. J., & Pearson, A. (2019). Archaeal lipid biomarker constraints on the Paleocene-Eocene carbon isotope excursion. *Nature Communications*, *10*(1), 4519. https://doi.org/10.1038/s41467-019-12553-3
Farley, K. A., & Eltgroth, S. F. (2003). An alternative age model for the Paleocene-Eocene thermal maximum using extraterrestrial ^{3}He. *Earth and Planetary Science Letters*, *208*(3–4), 135–148. https://doi.org/10.1016/S0012-821X(03)00017-7
Frieling, J., Svensen, H. H., Planke, S., Cramwinckel, M. J., Selnes, H., & Sluijs, A. (2016). Thermogenic methane release as a cause for the long duration of the PETM. *Proceedings of the National Academy of Sciences of the United States of America*, *113*(43), 12059–12064. https://doi.org/10.1073/pnas.1603348113
Galeotti, S., Krishnan, S., Pagani, M., Lanci, L., Gaudio, A., Zachos, J. C., et al. (2010). Orbital chronology of early eocene hyperthermals from the Contessa Road section, central Italy. *Earth and Planetary Science Letters*, *290*(1–2), 192–200. https://doi.org/10.1016/j.epsl.2009.12.021
Gingerich, P. D. (2019). Temporal scaling of carbon emission and accumulation rates: Modern anthropogenic emissions compared to estimates of PETM onset accumulation. *Paleoceanography and Paleoclimatology*, *34*(3), 329–335. https://doi.org/10.1029/2018PA003379
Giusberti, L., Coccioni, R., Sprovieri, M., & Tateo, F. (2009). Perturbation at the sea floor during the paleocene-eocene thermal maximum: Evidence from benthic foraminifera at Contessa Road, Italy. *Marine Micropaleontology*, *70*(3–4), 102–119. https://doi.org/10.1016/j.marmicro.2008.11.003
Giusberti, L., Rio, D., Agnini, C., Backman, J., Fornaciari, E., Tateo, F., & Oddone, M. (2007). Mode and tempo of the Paleocene- eocene thermal maximum from the Venetian pre-alps. *Geological Society of America Bulletin*, *119*(3–4), 391–412. https://doi.org/10.1130/B25994.1
Gutjahr, M., Ridgwell, A., Sexton, P. F., Anagnostou, E., Pearson, P. N., Pälike, H., et al. (2017). Very large release of mostly volcanic carbon during the Palaeocene-Eocene Thermal Maximum. *Nature*, *548*(7669), 573–577. https://doi.org/10.1038/nature23646
Haynes, L. L., & Hönisch, B. (2020). The seawater carbon inventory at the paleocene–eocene thermal maximum. *Proceedings of the National Academy of Sciences of the United States of America*, *117*, 24088–24095. https://doi.org/10.1073/pnas.2003197117
IPCC. (2021). *Climate Change 2021: The Physical Science Basis. Contribution of Working Group I to the Sixth Assessment Report of the Intergovernmental Panel on Climate Change*. In V. Masson-Delmotte, P. Zhai, A. Pirani, S. L. Connors, C. Péan, S. Berger, et al., (Eds.), (pp. 2391). Cambridge University Press. https://doi.org/10.1017/9781009157896
Kender, S., Bogus, K., Pedersen, G. K., Dybkjær, K., Mather, T. A., Mariani, E., et al. (2021). Paleocene/Eocene carbon feedbacks triggered by volcanic activity. *Nature Communications*, *12*, 1–10. https://doi.org/10.1038/s41467-021-25536-0
Kirtland Turner, S., Hull, P. M., Kump, L. R., & Ridgwell, A. (2017). A probabilistic assessment of the rapidity of PETM onset. *Nature Communications*, *8*(1), 353. https://doi.org/10.1038/s41467-017-00292-2
Komar, N., & Zeebe, R. E. (2017). Redox-controlled carbon and phosphorus burial: A mechanism for enhanced organic carbon sequestration during the PETM. *Earth and Planetary Science Letters*, *479*, 71–82. https://doi.org/10.1016/j.epsl.2017.09.011
Li, M., Bralower, T. J., Kump, L. R., Self-Trail, J. M., Zachos, J. C., Rush, W. D., & Robinson, M. M. (2022). Astrochronology of the paleocene-eocene thermal maximum on the Atlantic coastal plain. *Nature Communications*, *13*(1), 5618. https://doi.org/10.1038/s41467-022-33390-x
Littler, K., Röhl, U., Westerhold, T., & Zachos, J. C. (2014). A high-resolution benthic stable-isotope record for the South Atlantic: Implications for orbital-scale changes in Late Paleocene-Early Eocene climate and carbon cycling. *Earth and Planetary Science Letters*, *401*, 18–30. https://doi.org/10.1016/j.epsl.2014.05.054
Lord, N. S., Ridgwell, A., Thorne, M. C., & Lunt, D. J. (2016). An impulse response function for the "long tail" of excess atmospheric CO_2 in an Earth system model. *Global Biogeochemical Cycles*, *30*(1), 2–17. https://doi.org/10.1002/2014GB005074
Lyons, S. L., Baczynski, A. A., Babila, T. L., Bralower, T. J., Hajek, E. A., Kump, L. R., et al. (2019). Palaeocene-Eocene Thermal Maximum prolonged by fossil carbon oxidation. *Nature Geoscience*, *12*(1), 54–60. https://doi.org/10.1038/s41561-018-0277-3
Ma, Z., Gray, E., Thomas, E., Murphy, B., Zachos, J. C., & Paytan, A. (2014). Carbon sequestration during the Palaeocene-Eocene Thermal Maximum by an efficient biological pump. *Nature Geoscience*, *7*(5), 382–388. https://doi.org/10.1038/ngeo2139
Matthews, H. D., Gillett, N. P., Stott, P. A., & Zickfeld, K. (2009). The proportionality of global warming to cumulative carbon emissions. *Nature*, *459*(7248), 829–832. https://doi.org/10.1038/nature08047
McInerney, F. A., & Wing, S. L. (2011). The Paleocene-Eocene thermal maximum: A perturbation of carbon cycle, climate, and biosphere with implications for the future. *Annual Review of Earth and Planetary Sciences*, *39*(1), 489–516. https://doi.org/10.1146/annurev-earth-040610-133431
Montenegro, A., Brovkin, V., Eby, M., Archer, D., & Weaver, A. J. (2007). Long term fate of anthropogenic carbon. *Geophysical Research Letters*, *34*(19), L19707. https://doi.org/10.1029/2007GL030905
Murphy, B. H., Farley, K. A., & Zachos, J. C. (2010). An extraterrestrial ^{3}He-based timescale for the Paleocene-Eocene thermal maximum (PETM) from Walvis Ridge, IODP Site 1266. *Geochimica et Cosmochimica Acta*, *74*(17), 5098–5108. https://doi.org/10.1016/j.gca.2010.03.039
Penman, D. E., Caves Rugenstein, J. K., Ibarra, D. E., & Winnick, M. J. (2020). Silicate weathering as a feedback and forcing in Earth's climate and carbon cycle. *Earth-Science Reviews*, *209*, 103298. https://doi.org/10.1016/j.earscirev.2020.103298
Penman, D. E., Kirtland Turner, S., Sexton, P. F., Norris, R. D., Dickson, A. J., Boulila, S., et al. (2016). An abyssal carbonate compensation depth overshoot in the aftermath of the Palaeocene-Eocene Thermal Maximum. *Nature Geoscience*, *9*(8), 575–580. https://doi.org/10.1038/ngeo2757
Penman, D. E., & Zachos, J. C. (2018). New constraints on massive carbon release and recovery processes during the Paleocene-Eocene Thermal Maximum. *Environmental Research Letters*, *13*(10), 105008. https://doi.org/10.1088/1748-9326/aae285
Piedrahita, V. A., Galeotti, S., Zhao, X., Roberts, A. P., Rohling, E. J., Heslop, D., et al. (2022). Orbital phasing of the Paleocene-Eocene thermal maximum. *Earth and Planetary Science Letters*, *598*, 117839. https://doi.org/10.1016/j.epsl.2022.117839

Piedrahita, V. A., Heslop, D., Roberts, A. P., Rohling, E. J., Galeotti, S., Florindo, F., & Li, J. (2025). Data for: Assessing the duration of the Paleocene-Eocene thermal maximum [Dataset]. *Figshare*. https://doi.org/10.6084/m9.figshare.28560221.v1

Piedrahita, V. A., Zhao, X., Roberts, A. P., Rohling, E. J., Heslop, D., Galeotti, S., et al. (2023). Ocean acidification and carbon sequestration timescales following Paleocene-Eocene carbon cycle perturbations. *Earth and Planetary Science Letters*, *604*, 117992. https://doi.org/10.1016/j.epsl.2023.117992

Pogge von Strandmann, P. A., Jones, M. T., West, A. J., Murphy, M. J., Stokke, E. W., Tarbuck, G., et al. (2021). Lithium isotope evidence for enhanced weathering and erosion during the Paleocene-Eocene Thermal Maximum. *Science Advances*, *7*(42), eabh4224. https://doi.org/10.1126/sciadv.abh4224

Rogner, H. H. (1997). An assessment of world hydrocarbon resources. *Annual Review of Environment and Resources*, *22*(1), 217–262. https://doi.org/10.1146/annurev.energy.22.1.217

Röhl, U., Bralower, T. J., Norris, R. D., & Wefer, G. (2000). New chronology for the late Paleocene thermal maximum and its environmental implications. *Geology*, *28*(10), 927–930. https://doi.org/10.1130/0091-7613(2000)28<927:NCFTLP>2.0.CO;2

Röhl, U., Westerhold, T., Bralower, T. J., & Zachos, J. C. (2007). On the duration of the Paleocene-Eocene thermal maximum (PETM). *Geochemistry, Geophysics, Geosystems*, *8*(12), Q12002. https://doi.org/10.1029/2007GC001784

Secord, R., Bloch, J. I., Chester, S. G., Boyer, D. M., Wood, A. R., Wing, S. L., et al. (2012). Evolution of the earliest horses driven by climate change in the Paleocene-Eocene Thermal Maximum. *Science*, *335*(6071), 959–962. https://doi.org/10.1126/science.1213859

Solomon, S., Plattner, G. K., Knutti, R., & Friedlingstein, P. (2009). Irreversible climate change due to carbon dioxide emissions. *Proceedings of the National Academy of Sciences of the United States of America*, *106*(6), 1704–1709. https://doi.org/10.1073/pnas.0812721106

Thomas, E. (1990). Late cretaceous through neogene deep-sea benthic foraminifera (Maud Rise, Weddell sea, Antarctica). *Proceedings of the Ocean Drilling Program, Scientific Results*, *113*, 571–594. https://doi.org/10.2973/odp.proc.sr.113.123.1990

Torfstein, A., Winckler, G., & Tripati, A. (2010). Productivity feedback did not terminate the Paleocene-Eocene Thermal Maximum (PETM). *Climate of the Past*, *6*(2), 265–272. https://doi.org/10.5194/cp-6-265-2010

van der Meulen, B., Gingerich, P. D., Lourens, L. J., Meijer, N., van Broekhuizen, S., van Ginneken, S., & Abels, H. A. (2020). Carbon isotope and mammal recovery from extreme greenhouse warming at the Paleocene-Eocene boundary in astronomically-calibrated fluvial strata, Bighorn Basin, Wyoming, USA. *Earth and Planetary Science Letters*, *534*, 116044. https://doi.org/10.1016/j.epsl.2019.116044

Westerhold, T., Marwan, N., Drury, A. J., Liebrand, D., Agnini, C., Anagnostou, E., et al. (2020). An astronomically dated record of Earth's climate and its predictability over the last 66 million years. *Science*, *369*(6509), 1383–1387. https://doi.org/10.1126/science.aba6853

Westerhold, T., Röhl, U., Donner, B., McCarren, H. K., & Zachos, J. C. (2011). A complete high-resolution Paleocene benthic stable isotope record for the central Pacific (ODP Site 1209). *Paleoceanography*, *26*(2). https://doi.org/10.1029/2010PA002092

Westerhold, T., Röhl, U., Donner, B., & Zachos, J. C. (2018). Global extent of early Eocene hyperthermal events: A new Pacific benthic foraminiferal isotope record from Shatsky Rise (ODP site 1209). *Paleoceanography and Paleoclimatology*, *33*(6), 626–642. https://doi.org/10.1029/2017PA003306

Westerhold, T., Röhl, U., Laskar, J., Raffi, I., Bowles, J., Lourens, L. J., & Zachos, J. C. (2007). On the duration of magnetochrons C24r and C25n and the timing of early Eocene global warming events: Implications from the Ocean Drilling Program Leg 208 Walvis Ridge depth transect. *Paleoceanography*, *22*(2), PA2201. https://doi.org/10.1029/2006PA001322

Westerhold, T., Röhl, U., Wilkens, R. H., Gingerich, P. D., Clyde, W. C., Wing, S. L., et al. (2018). Synchronizing early Eocene deep-sea and continental records-cyclostratigraphic age models for the Bighorn Basin Coring Project drill cores. *Climate of the Past*, *14*(3), 303–319. https://doi.org/10.5194/cp-14-303-2018

Wing, S. L., Harrington, G. J., Smith, F. A., Bloch, J. I., Boyer, D. M., & Freeman, K. H. (2005). Transient floral change and rapid global warming at the Paleocene-Eocene boundary. *Science*, *310*(5750), 993–996. https://doi.org/10.1126/science.1116913

Zachos, J. C., Röhl, U., Schellenberg, S. A., Sluijs, A., Hodell, D. A., Kelly, D. C., et al. (2005). Rapid acidification of the ocean during the Paleocene-Eocene thermal maximum. *Science*, *308*(5728), 1611–1615. https://doi.org/10.1126/science.1109004

Zeebe, R. E. (2013). Time-dependent climate sensitivity and the legacy of anthropogenic greenhouse gas emissions. *Proceedings of the National Academy of Sciences of the United States of America*, *110*(34), 13739–13744. https://doi.org/10.1073/pnas.1222843110

Zeebe, R. E., & Lourens, L. J. (2019). Solar system chaos and the Paleocene-Eocene boundary age constrained by geology and astronomy. *Science*, *365*(6456), 926–929. https://doi.org/10.1126/science.aax0612

Zeebe, R. E., Ridgwell, A., & Zachos, J. C. (2016). Anthropogenic carbon release rate unprecedented during the past 66 million years. *Nature Geoscience*, *9*(4), 325–329. https://doi.org/10.1038/ngeo2681

Zeebe, R. E., Westerhold, T., Littler, K., & Zachos, J. C. (2017). Orbital forcing of the Paleocene and Eocene carbon cycle. *Paleoceanography*, *32*(5), 440–465. https://doi.org/10.1002/2016PA003054

Zeebe, R. E., & Zachos, J. C. (2013). Long-term legacy of massive carbon input to the Earth system: Anthropocene versus Eocene. *Philosophical Transactions of the Royal Society A*, *371*(2001), 20120006. https://doi.org/10.1098/rsta.2012.0006

Zeebe, R. E., Zachos, J. C., & Dickens, G. R. (2009). Carbon dioxide forcing alone insufficient to explain Palaeocene-Eocene Thermal Maximum warming. *Nature Geoscience*, *2*(8), 576–580. https://doi.org/10.1038/ngeo578